Iranian Journal of Medical Physics

ijmp.mums.ac.ir

Optimization of Imaging Parameters in Micro-CT Scanner Based On Signal-To-Noise Ratio for the Analysis of Urinary Stone Composition

Leni Aziyus Fitri [1*], Yuni Warty [1], Freddy Haryanto [1], Umar Fauzi [1], Fourier Latief [1]

1. Institute Teknologi Bandung, Bandung, West Java, 40132, Indonesia

ARTICLE INFO

Article type:
Original Article

Article history:
Received: Feb 08, 2019
Accepted: Jul 12, 2019

Keywords:
Imaging Parameters
Micro CT
Optimization
SNR
Urinary Stone

ABSTRACT

Introduction: Micro-CT scanner with a resolution of about 5 micrometers is one of the modalities used to create three-dimensional/two-dimensional images of urinary stones. This study aimed to optimize imaging parameters in micro-computed tomography (CT) scanner based on the signal-to-noise ratio (SNR) of urinary stones for the analysis of stone composition.
Material and Methods: In this study, eight micro-CT scanning protocols were applied to five urinary stones taken from different patients. Each scanning protocol had different voltage, current, and exposure parameters. The reconstructed images were then analyzed based on image brightness and SNR. The optimized imaging parameters which were chosen were that having high SNR because the high-quality image has high SNR.
Results: The results showed that two groups of urinary stones had the same mean Hounsfield Units (HU) value in the third scanning protocols (i.e., 65 kV, 123 µA, and 850 ms). Mean HU values in group one (i.e., stones numbered 1, 3, and 4) were reported as 790, 760, and 720, respectively. The second group (i.e., stones numbered 2 and 5) had mean HU values of -514 and -343, respectively. The imaging parameters (i.e., 75 kV, 106 µA, and 600 ms) had high SNR (25-34) for the first group. The SNR (12.8-13.25) was for the second group at imaging parameters (i.e., 85 kV, 94 µA, and 500 ms).
Conclusion: Based on the SNR, the two optimal imaging parameters for the first and second groups were reported as 75 kV, 106 µA, and 600 ms, as well as 85 kV, 94 µA, and 500 ms, respectively.

►*Please cite this article as:*
Fitri LA, Warty Y, Haryanto F, Fauzi U, Latief F. Optimization of Imaging Parameters in Micro-CT Scanner Based On Signal-To-Noise Ratio for the Analysis of Urinary Stone Composition. Iran J Med Phys 2020; 17: 153-160. 10.22038/ijmp.2019.37851.1482.

Introduction

Urinary stone is the deposition of minerals and organic compounds in the human urinary tract (i.e., kidney, ureter, and bladder) [1]. The most common type of urinary stones is calcium-containing stones; other types include cystine, struvite, and uric acid (UA) [2, 3]. Table 1 tabulates the distinctions of each stone based on the mass density values of chemical composition. When a urinary stone moves around within the kidney or passes into the ureter, some symptoms will be present, such as severe pain in the side and back, pain on urination, red or brown urine, nausea, and vomiting [4]. Increasing incidence and prevalence of kidney stones is a growing concern in Asia included Indonesia. Market information compiled by Cook Medical (February 2016) showed that the rate of incidence was 0.3% [5].

Some treatments for the removal of urinary stones from the human urinary tract are medical therapy, shockwave lithotripsy, ureteroscopy, and percutaneous nephrolithotomy (PCNL) [4]. Treatment of urinary stones varies depending on the type of stone for the reduction of severe complications and recurrence, especially in noncalcium stones. The PCNL includes several risks, such as higher blood loss, increased radiation, urine leak, or pain [6]. The PCNL is an effective modality for the treatment of calcium and large stones [7]. However, noncalcium stones, such as UA and struvite, can be removed through medically or shockwave lithotripsy [8].

Use of computed tomography (CT) scan images for determining the type of urinary stones has been studied in previous studies. Liden (2018) differentiated pure UA from other types of urinary stone using the peak attenuation of CT images [9]. A prediction model based on parameters (i.e., body mass index and stone diameter) was developed by Park (2016) for shockwave lithotripsy treatment [10]. Stone size and composition of urinary stones were evaluated by Stewart (2015) based on Hounsfield Units (HU) on noncontrasted CT scan images [11].

Wisenbaugh (2014) demonstrated the limitation of CT HUs in predicting mixed stone composition [8]. In a study carried out by Fitri (2016), the urinary stones were identified by dual-energy micro-CT SkyScan 1173 [12].

*Corresponding Author: Tel: +62-812-6732-7107; E-mail: leniaziyus@s.itb.ac.id

Table 1. Mass density of urinary stones

Type of bladders		Chemical Formula	Mass density (g/cm^3)
Calcium oxalate	Mixture	$CaC_2O_4.3H_2O$	1.85
Cystine	Compound	$C_3H_7NO_2S$	1.293
Struvite	Mixture	$NH_4MgPO_4.6H_2O$	1.7
Uric acid	Compound	$C_5H_4N_4O_3$	1.85

Ananthakrisnan (2018) showed that dual-layer spectral detector differentiated the pure UA from nonUA stones ex vivo [13]. On the other hand, Hokamp (2018) used semiautomatic segmentation for the characterization of the kidney stones image [14].

However, the results of above-mentioned studies have not been able to distinguish the types of cystine and struvite stones because the HUs of the two stones are overlapping at high energy levels. Nonetheless, based on the mass density in Table 1, both stones (i.e., cystine and struvite) have different mass densities (i.e., 1.293 and 1.7 g/cm^3). Appropriate imaging parameters will be able to distinguish the type of stones based on HU because their mass densities are different. Therefore, it is necessary to investigate the optimization of imaging parameters in micro-CT scan [15, 16] to analyze the composition of urinary stones [9].

The X-ray microtomography or micro-CT SkyScan 1173 classified as a laboratory cone beam scanner with a maximum resolution of 5 µm/pixel [17]. Micro-CT has a very small focal spot (<5 µm) on the anode target, a rotational subject holder, and a flat panel detector [18, 19]. Source of micro-CT, X-ray penetrates and interacts depending on the source energy and electron density of the material [20]. The micro-CT scanner is an ideal solution for the analysis of the microstructure due to its nondestructive nature [21-26]. Micro-CT was also used to determine the composition of urinary stones [12]. This study aimed to optimize imaging parameters in micro-CT scanner based on the signal-to-noise-ratio (SNR) of urinary stones for analyzing stone composition because the SNR largely determines the image quality.

Materials and Methods

Five urinary stones with a diameter of 5-15 mm were used as the samples obtained from different patients by a surgical procedure. Figure 1 shows the procedure of the optimization of imaging parameters in micro CT. Analyses of the stones were conducted both qualitatively and quantitatively. The qualitative analysis was performed by observing the samples based on the image brightness for the determination of the homogeneous area. Region of interest (ROI) was drawn in the two-dimensional (2D) urinary stone image by referring to the homogeneous area.

Subsequently, the quantitative analysis was carried out using the equation to calculate the SNR of the image because SNR determines the image quality. Quantitative analysis of urinary stone images referred to a study conducted by Pratt (2017) where the appropriate parameters were based on the high SNR of the image [27].

Data Acquisition

Urinary stones were scanned and rotated +180° using micro-CT (SkyScan 1173, Bruker, Belgium) for the creation of projection images. High energy and micro-focus X-ray of the SkyScan 1173 was used to achieve higher stability on the focal spot position. The scanner has also a flat panel sensor with larger format (i.e., >5 Mp) and fiber-optic window with a glass from lead [28].

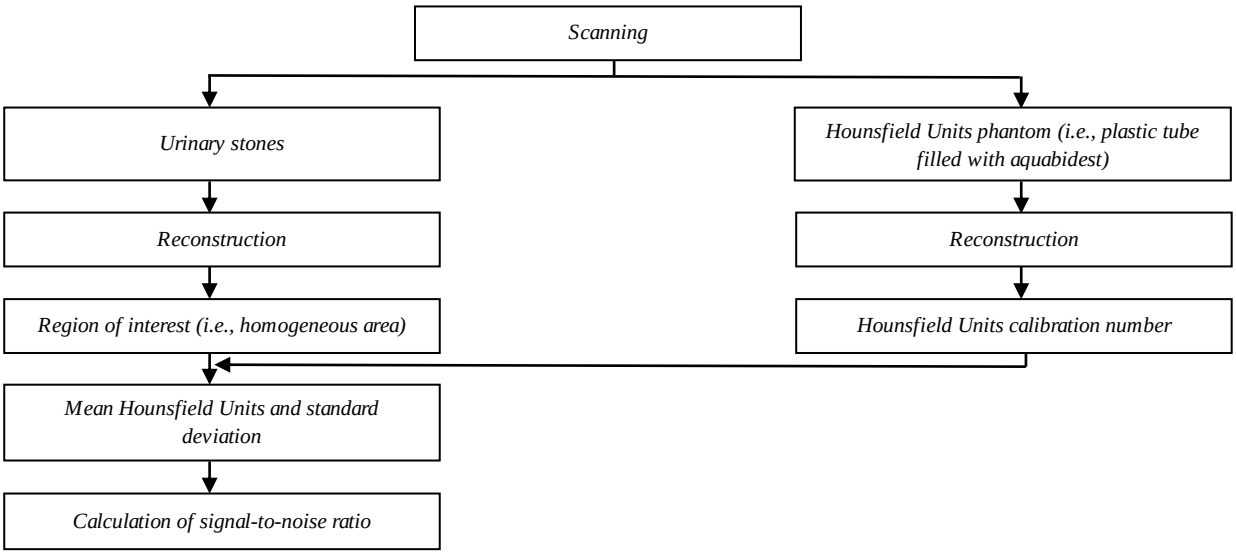

Figure 1. Study procedure the optimization of imaging parameters in micro CT

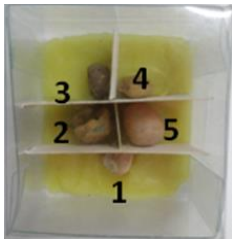

Figure 2. Arrangement of urinary stones samples

The samples were arranged in a transparent box coated with plasticine at the bottom as shown in Figure 2. The arranged samples in Figure 2 were scanned by eight scanning protocols each of which had different parameters related to the variation of source voltage, source current, and exposure time. However, the pixel size (i.e., 13.89 µm) and filter type (i.e., Al 1 mm) were maintained for every protocol. The object-scanning scheme is shown in Figure 3; nevertheless, the results of the scanning protocols are shown in Table 2.

Figure 3 depicts the samples placed on a holder that can rotate up to 360°. A 240° rotation (known as +180° rotation) was used in the present study [29]. The object distances to the source and detector were 101.41 and 262.59 mm, respectively, resulting in a spatial resolution of 13.89 µm/pixel. This distance was constant for all scanning protocols. Scanning was conducted using a flat panel detector with 50 µm pixel size with 2240 × 2240 pixel dimension. The total scanning time was different for each scanning protocol within the range of 2-5.5 h. The scan duration was determined by the exposure time, rotation step, and total angle of rotation.

Reconstruction

The image was reconstructed using NReconstruction (NRecon) software (version 1.7.1.0, Bruker, Belgium). The correction values (reconstruction parameters) were applied in the image to reduce beam hardening effect, ring artifact, and noise. The correction values were beam hardening of 8, ring artifacts of 15, and smoothing of 1. The reconstructed image had the same isotropic spatial resolution as the projection image (i.e., 13.89 µm/pixel).

Analysis

The analyses were conducted both qualitatively and quantitatively using CT Analyser (version 1.16.4.1, Bruker, Belgium). There were two analytical stages, including (1) binary selection threshold and (2) calibration to the HU value of water. A binary image is an image with only two intensity levels (i.e., black and white) from an original grayscale digital image. Binary selection threshold is a stage to select object area (i.e., white) and background area (i.e., black) based on the histogram [28]. The histogram has a deep and sharp valley between two peaks; therefore, the threshold was chosen at the bottom of this valley [30, 31].

The HU calibration was derived from aquabidest scanned using the same parameters for all object scanning protocols. There were 6 steps for the calibration of density using HU. Firstly, micro-CT scanned HU phantom (i.e., a plastic tube filled with aquabidest) using the same parameters for all object scanning protocols and NRecon software (version 1.7.1.0, Bruker, Belgium) reconstructed projection images. Secondly, CT-An software analyzed the reconstructed dataset of the HU phantom and measured the mean grayscale value of HU phantom from the ROI of the reconstructed dataset. Then, the values (i.e., 0 for minimum grayscale and -1000 for minimum HU) were entered in density calibration panel. The maximum grayscale and maximum HU were entered the measured mean grayscale value of HU phantom and 0, respectively. The HU calibration number was obtained after calibration [28].

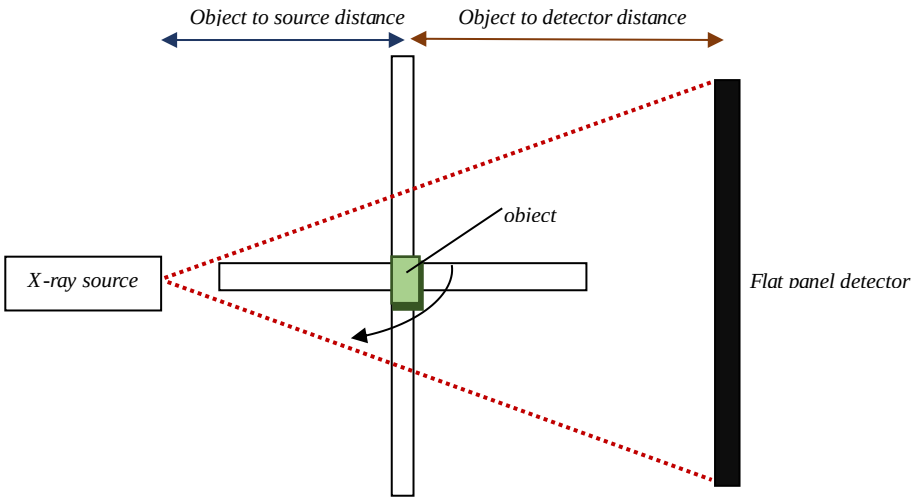

Figure 3. Scanning scheme [29]

Table 2. Scanning protocols (i.e., imaging parameters) of urinary stones in micro-computed tomography SkyScan 1173

Protocol	Source voltage (kV)	Source current (µA)	Exposure (ms)
1	45	177	1500
2	55	145	1200
3	65	123	850
4	75	106	600
5	85	94	500
6	95	60	500
7	105	50	500
8	115	50	500

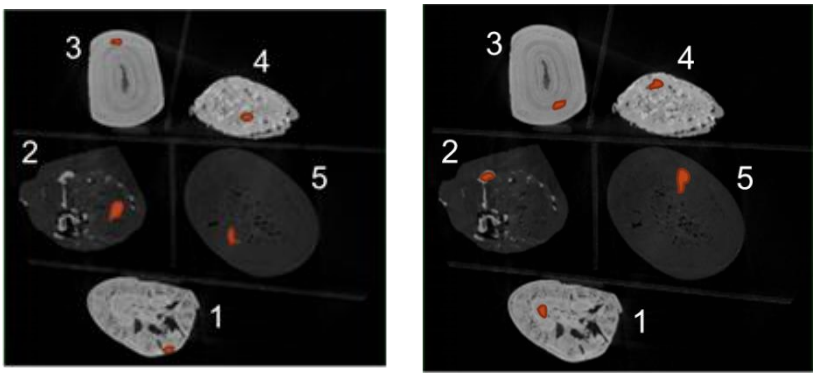

ROI 1 ROI 2

Figure 4. Regions of interest 1 and 2 related to each urinary stone image

Results

Each scanning protocol produced 1200 projection images in a 16-bit tagged image file format. Figure 5 shows that the first scanning protocol (i.e., 45 kV of source voltage, 177 µA, and 1500 ms of exposure time) produced darker projection image than the eighth scanning protocol (i.e., 115 kV of source voltage, 50 µA, and 500 ms of exposure time). Nevertheless, in order to obtain the complete information of the object, the reconstruction requires to be performed on the projection image from the entire rotation step. Figure 6 depicts the example of reconstructed images at the vertical slice position of 14.535 mm.

Reconstruction image of each scanning protocol (i.e., imaging parameters) had different brightness. Figure 6 illustrates that the first scanning protocol (i.e., 45 kV of source voltage, 177 µA, and 1500 ms of exposure time) produced the brightest reconstructed image. However, the noise on that image obtained by the first scanning protocol was higher, compared to that of other images.

Observation of the brightness of the reconstructed images indicated that the two groups of stones were visually similar. The first group consisted of the stones numbered 1, 3, and 4. In addition, the second group comprised of the stones numbered 2 and 5. Stone numbered 2 had white and black regions; however, stone numbered 5 was black in almost every scanning protocol.

Figure 7 shows both ROI 1 and 2 that represent the mean HU value of each stone. Mean HU value of each stone decreased at the second scanning protocol (i.e., 55 kV of source voltage, 145 µA of source current, and 1200 ms of exposure time), fifth scanning protocol (i.e., 85 kV of source voltage, 94 µA of source current, and 500 ms of exposure time), and seventh scanning protocol (i.e., 105 kV of source voltage, 50 µA of source current, and 500 ms of exposure time).

The stones can be divided into two groups by analyzing the mean HU value of two ROI in Figure 7. The first group consisted of stones numbered 1, 3, and 4 with generally higher mean HU value, and the second group included stones numbered 2 and 5 with generally lower mean HU value. Nonetheless, stones numbered 2 and 5 were mixture stones because they had a variation in mean HU values on ROI 1.

Figure 8a illustrates that the standard deviation of each stone is high at the first scanning protocol (i.e., 45 kV of source voltage, 177 µA, and 1500 ms of exposure time). The eighth scanning protocol (i.e., 115 kV of source voltage, 50 µA, and 500 ms of exposure time) obtained the lowest standard deviation. Figure 8a and 8b also show the low standard deviation at the fifth scanning protocol (i.e., 85 kV of source voltage, 94 µA of source current, and 500 ms of exposure time).

Quantitative analysis of this study was conducted by the calculation of the SNR value. Figure 9 depicts the relationship between SNRs and scanning protocols (i.e., imaging parameters). The SNR of each stone fluctuated in the present study. Figure 9a shows that the first group (i.e., stones numbered 1, 3, and 4) has the maximum SNR at the fourth scanning protocol (i.e., 75 kV of source voltage, 106 µA of source current, and 600 ms of exposure time). The SNR of the second group (i.e., stone numbered 2 and 5) was at the maximum level at the fifth scanning protocol (i.e., 85 kV of source voltage, 94s µA of source current, and 500 ms of exposure time).

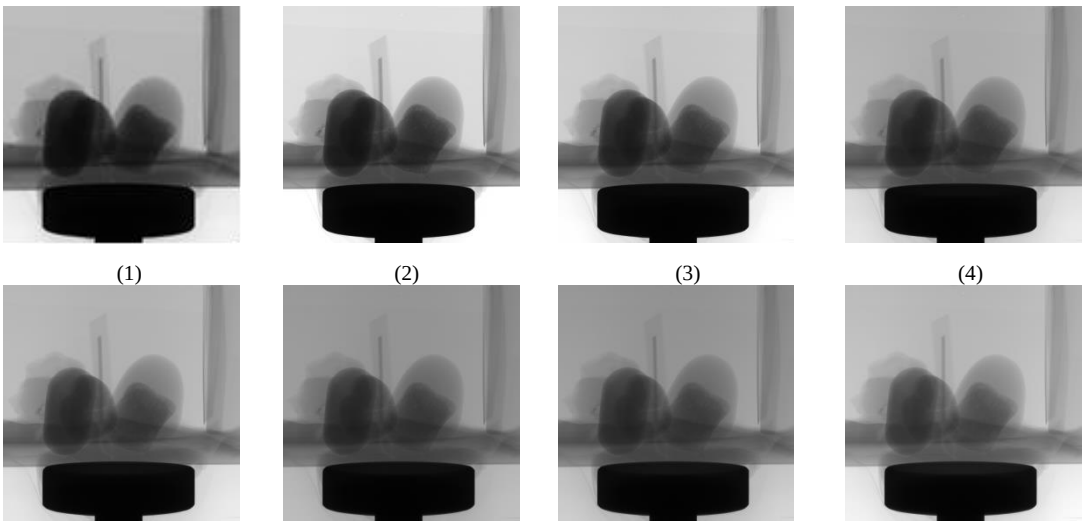

Figure 5. Projection images of all scanning protocols; counterclockwise 0.2° rotation of images

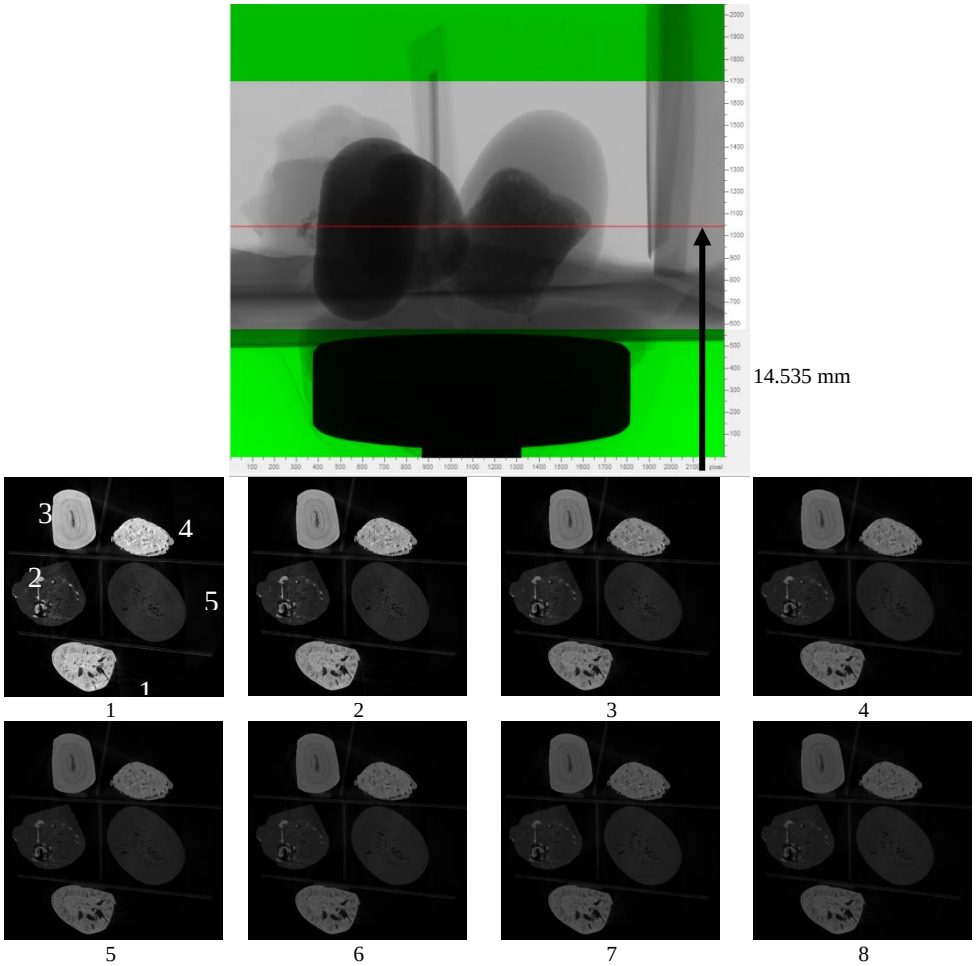

Figure 6. Reconstructed images of all scanning protocols at the vertical slice position of 14.535 mm

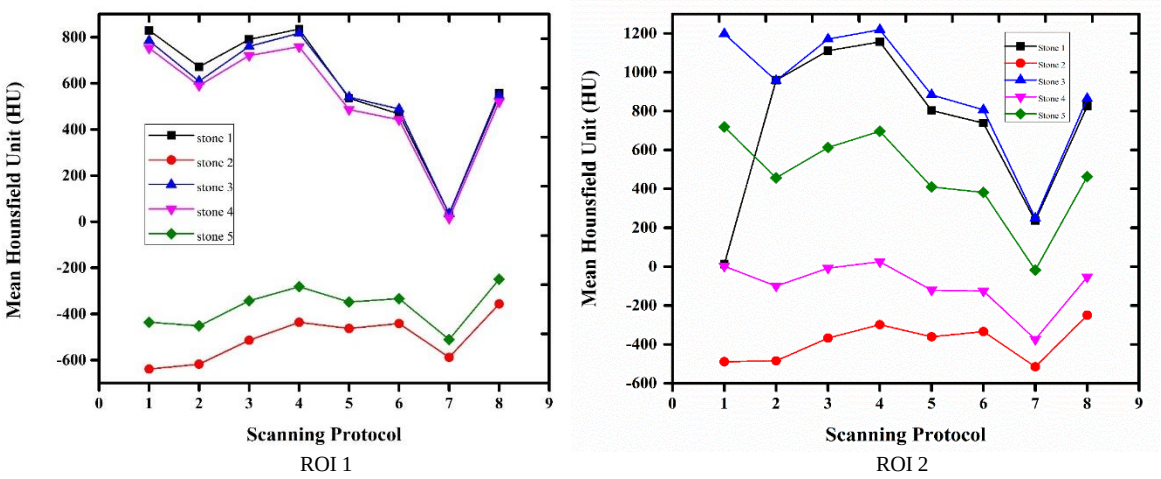

ROI 1 ROI 2

Figure 7. Mean Hounsfield Unit of five urinary stones on regions of interest 1 and 2

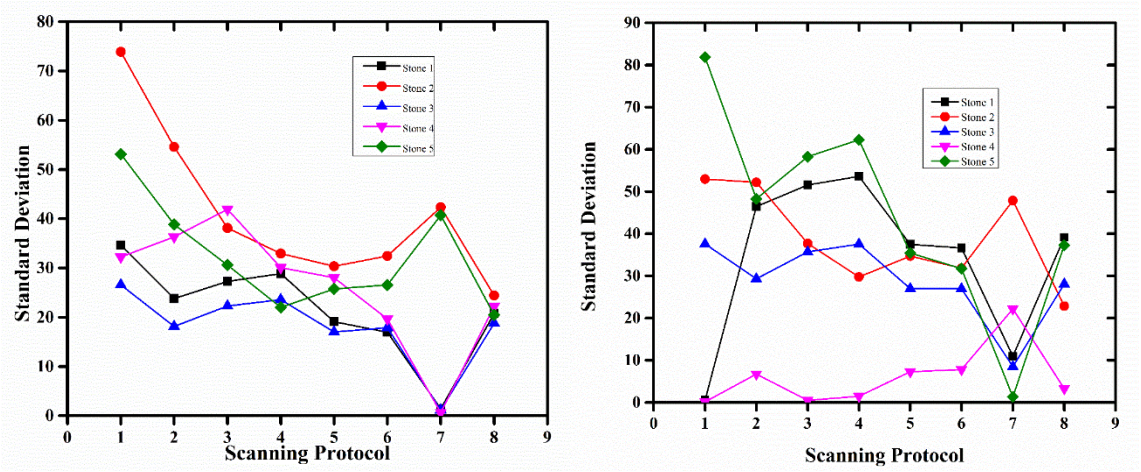

ROI 1 ROI 2

Figure 8. Relationship between standard deviation and scanning protocols (i.e., imaging parameters)

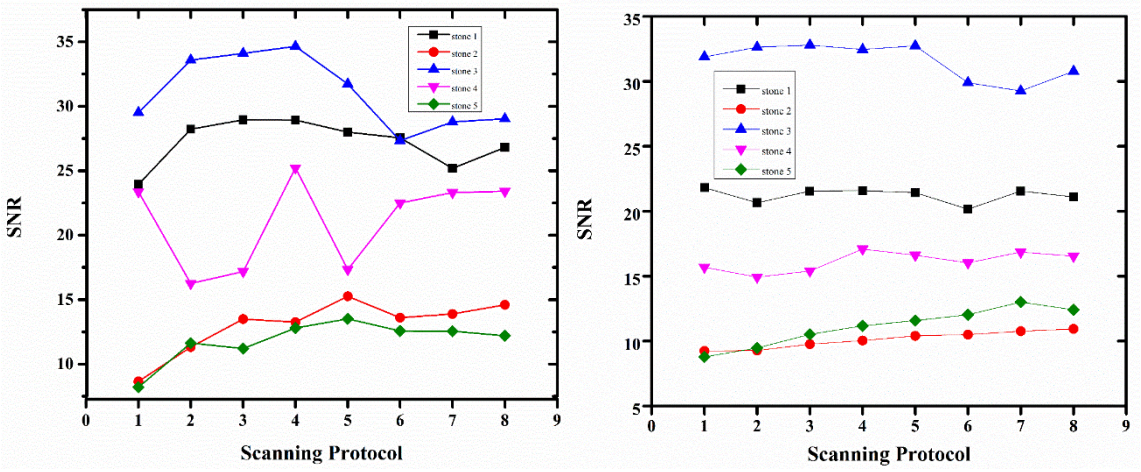

ROI 1 ROI 2

Figure 9. Relationship between signal-to-noise ratios (SNRs) and scanning protocols (i.e., imaging parameters)

Figure 9b illustrates that the maximum SNR of the first group was the fifth scanning protocol (i.e., 85 kV of source voltage, 94 µA of source current, and 500 ms of exposure time).

Discussion

This study obtained the optimization of imaging parameters in micro-CT SkyScan 1173 based on SNR for the analysis of urinary stone composition. The imaging parameters (i.e., source voltage, source current, and exposure time) are the parameters that determine the X-ray beam characteristics (i.e., quality and quantity). The source voltage accelerates the electrons from the cathode filament toward anode. The source current is the rate of electron flow from the cathode to anode. The exposure time is the duration of X-ray production [32].

Based on the HU values, urinary stones can be classified into calcium oxalate, cystine, struvite, and UA [33]. The classification based on the HU value describes the attenuation of the X-ray related to the electron density and amount of energy transmitted [34]. The results showed that the two groups of urinary stones had the same mean HU values. Group one consisted of stones numbered 1 (790), 3 (760), and 4 (720). Then, the stones numbered 2 (-514) and 5 (-343) were considered the second group.

Brightness differences of the reconstructed images of all scanning protocols were due to the influence of the source voltage and electron density. By obtaining the appropriate X-ray voltage parameters, the scanning process produces high-quality images [17] that is in line with the results of a study conducted by Hermanek (2017) [35]. By increasing the source voltage, image noise decreases, and the images have a better contrast ratio [36-38].

Quantitatively, Figure 9a shows that the relationships between SNRs and scanning protocols (i.e., imaging parameters) have peaks because saturation occurs at certain source voltage. Theoretically, the low exposure levels produce images with relatively low SNR. Exposure depends on both the quantity and quality of the X-Ray beam. Source voltage determines the quantity, quality (i.e., penetrability), and transmission through the object; however, source current determines only the quantity [32, 38]. The optimized imaging parameters, which were chosen, were parameters obtaining high SNR because high SNR value is one of the characteristics of image quality [39, 40]. This result is in accordance with the findings of a study carried out by Lid et al. [13].

Conclusion

The four scanning protocols (i.e., the first until fourth) increased the SNR value of the first group by 30%. Nevertheless, SNR decreased 20% at the scanning protocol fifth until the seventh source. Based on SNR, the optimizations of imaging parameters were 75 kV and 115 kV of source voltage. Based on the SNR, the two optimized imaging parameters for the first and second groups were 75 kV of source voltage, 106 of source current, and 600 ms of exposure time, as well as 85 kV of source voltage, 94 µA of source current, and 500 ms of exposure time, respectively.

Acknowledgment

The authors would like to express great appreciation to Scholarship Foundation, the Indonesia Endowment Fund for Education (LPDP). The authors would like to acknowledge Dr. Ridwan (RS. Hasan Sadikin Bandung) for providing five urinary stones and Faculty of Mathematics and Natural Sciences Institut Teknologi Bandung for scanning using micro-CT SkyScan.

References

1. Chatterjee P, Chakraborty A, Mukherjee AK. Phase composition and morphological characterization of human kidney stones using IR spectroscopy, scanning electron microscopy, and X-ray Rietveld analysis. Spectrochimia Acta Part A: Molecular and Biomolecular Spectroscopy. 2018; 200: 33-42.
2. Tseng TY, Preminger GM. Kidney stones: flexible ureteroscopy. Clinical Evidence. 2015; 10: 1-14.
3. Prywer J,Torzewska A. Impact of bacteria on aggregation of crystalline and amorphous components of infectious urinary stones. 2019; 506: 71-8.
4. Mayo clinic. Kidney Stone. 2019. Available from: https://www.mayoclinic.org/diseases-conditions/kidney-stones/symptoms-causes/syc-20355755.
5. Cook medical. World Kidney Day: A global look at a growing concern. 2016. Available from: https://www.cookmedical.com/urology/world-kidney-day-a-global-look-at-a-growing-concern/.
6. Ranabothu S, Bernstein AP, Drzewiech BA. Diagnosis and management of non-calcium-containing stones in the pediatric population. Int Urol and Nephrol. 2018; 50(7): 1191-8.
7. Vicentini FC, Perrella R, Souza VMG, Hisano M, Murta CB, Clamaro JF. Impact of patient position on the outcomes of percutaneous neprolithotomy for complex kidney stones. 2018; 44(5): 956-97.
8. Wisenbaugh ES, Paden RG, Silva AC, Humphhreys MR. Dual energy vs conventional computed tomography in determining stone composition. Urology. 2014; 83 (6): 1243-7.
9. Liden M. A new method for predicting uric acid composition in urinary stones using routine single energy. Urolithiasis. 2018; 46 (4): 325-33.
10. Park HS, Gong MK, Yoon GY, Moon DG, Cheon J, Choi YD. Computed tomography-based novel prediction model for the outcome of shockwave lithotripsy in proximal ureteral stones. J Endourol. 2016; 30 (7): 810-6.
11. Stewart G, Johnson L, Ganesh H, Davenport D, Smelser W, Crispen P, et al. Stone size limits the use of Hounsfield Units for prediction of calcium oxalate stone composition. Urology. 2015; 85 (2): 292-5.
12. Fitri LA, Asyana V, Ridwan T, Anwary F, Soekersi H, Latief FDE , et al. Dual energy micro-CT Skyscan 1173 was able to characterize the composition of the urinary stone. Journal of Physics: conference series. 2016; 694 (1): 1-5.

13. Ananthakrishnan L, Duan X, Xi Y, Lewis MA, Pearle M S, Antonenlli JA, et all. Dual-layer spectral detector CT: non-inferiority assesment compared to dual-source dual energy CT in discriminating uric acid from non-uric acid renal stones ex vivo. Abdom Radiol. 2018; 43(11): 3075-81.
14. Hokamp NG, Salem J, Hesse A, Holz JA, Ritter M, Heidenreich A, et al. Low-dose characterization of kidney stones using spectral detector computed tomography: an ex vivo study. Investigative radiology. 2018; 53(8):457-62.
15. Naseri S, Nezhad MM, Hozhabri Z, Haghparast A, karami G, Hejazi P. Optimization of parameters in 16-slice CT-scan protocols for reduction of the absorbed dose. Iran J Med Phys. 2014; 11 (2): 270-5.
16. Kalhor P, Changizi V, Hosseini A, Jazayeri E. Optimization of Head CT Protocol to Reduce the Absorbed Dose in Eye Lenses and Thyroid: A Phantom Study. Iran J Med Phys. 2019; 16 (1): 64-74.
17. Du Plessis A, Boshoff W P. A review of X-ray computed tomography of concrete and asphalt construction materials. Construction and Building Materials. 2019; 199: 637-51.
18. Lee SC, Kim HK, Chun IK, Cho MH, Lee SY, Cho MH. A flat-panel detector based micro-CT system: performance evaluation for small-animal imaging. Phys. Med. Biol. 2003; 48: 4173‑85.
19. Bultreys T, Boone AM, Boone NM, Schryver TD, Masschaele B, Hoorebeke LV, et al. Fast laboratory-based micro-computed tomography for pore-scale research: Illustrative experiments and perspectives on the future. Advances in Water Resources. 2016; 95: 341‑51.
20. Liu X, Wang J, Lu S, Ge L, Hu F, Li C, et al. Pore-scale characterization of tight sandstone in yanchang formation ordos basin China using micro-CT and SEM imaging from nm- to cm-scale. Fuel. 2017; 209: 254‑64.
21. Szewczykowski, PP, Skarzynski, L. Application of the X-ray micro-computed tomography to the analysis of the structure of polymetric materials. Polimery J. 2019; 64 (10): 12-22.
22. Koddenberg T, Krause KC, Krause A. Tomographic analysis of siliceous particulates in Australian turpentine wood (Syncarpia golulifera) through X-ray micro-computed tomography. Micron . 2019; 117: 22-8.
23. Wu H, Zhou Y, Yao Y, Wu K. Imaged based fractal characterization of micro-fracture structure in coal. Fuel J. 2018; 239: 53-62.
24. Takano N, Fukasawa K, Nishiyabu K. Structural strength prediction for porous titanium based on micro-stress concentration by micro-CT image-based multiscale simulation. Int J of Mech Scien. 2010; 52 (2): 229-35.
25. Gomila R, Arancibia G, Mery D, Nehler M, Bracke R, Morata D. Palaeopermeability anisotropy and geometrical properties of sealed-microfractures from micro-CT analyses: an open-source implementation. Micron J. 2019; 117: 29‑39.
26. Alexander SL, Rafaels K, Gunnarsson CA, Weerasooriya T. Structural analysis of the frontal and parietal bones of the human skull. J of Mechanical Behavior of Biomedical Materials. 2019; 90: 689-701.
27. Pratt R, Hutchinson JC, Melbourne A, Zuluaga MA, Virasami A, Vercauteren T, et al. Imaging the human placental microcirculation with micro-focus computed tomography: optimisation of tissue preparation and image acquisition. Placenta. 2017; 60: 36-9.
28. Bruker micro-CT. Applying Hounsfield unit density calibration in SkyScan CT-analyser. Bruker-microCT Method note. 2005: 1-5.
29. Zhu S, Tian J, Yan G, Qin C, Liu J. An experimental cone beam micro-CT system for small animal imaging. Int. J Biomed Imaging. 2009; 7258: 960573.
30. Prewitt JMS, Mendelsohn ML. The analysis of cell images. Ann. N.Y. Acad. Sci. 1966; 128: 1035-53.
31. Otsu N. A threshold selection method from gray-level histogram. IEE Transcations on Systems. 1979; 9: 62-6.
32. Bushberg JT, Seibert JA, Leidholdt EM, Boone JM. The Essential Physics of Medical Imaging. 2rd ed. USA: Lippincott Wiliams & Wilkins; 2002.
33. Lee JS, Cho KS, Lee SH, Yoon YE, Kang DH, Jeong WS, et al. Stone heterogeneity index on single-energy noncontrast computed tomography can be a positive predictor of urinary stone composition. Plos One. 2018; 13 (4): e0193945.
34. Wojcik GS. Determining the uncertainty of X-ray absorption measurements. J of Research of the National Institute of Standards and Technology. 2004; 109 (5).
35. Hermanek P, Carmignato S. Porosity measurements by X-ray computed tomography: accuracy evaluation using a calibrated object. Precision Engineering. 2017; 49: 377-87.
36. Toricelli FCM, Marchini GS, De S, Yamacake KGR, Mazzucchi E, Monga M. Predicting urinary stone composition based on single-energy non-contrast computed tomography: the challenge of cystine. Urology. 2014; 83 (6): 1258-64.
37. Du Plessis A, le Roux SG, Guelpa A. Comparison of medical and industrial X-ray computed tomography for non-destructive testing. case studies in nondestructive testing and evaluation. 2016; 6 (A): 17-25.
38. Albrecht MH, Bickford MW, Schoepf UJ, Tesche C, Santis DD, Eid M, et all. Beam-hardening in 70-kV coronary CT angiography: artifact reduction using an advanced post-processing algorithm. Eur J Radiol. 2018; 101: 111-7.
39. Davoodi M, Abadi SB, Andabili SHA, Kabir A. Comparison of image quality of low voltage 64-slice multidetector CT angiography with the standard condition in patients suspected of pulmonary embolism. Iran J Med Phys. 2018; 15 (4): 237-42.
40. Langkvist M, Jendeberg J, Thunberg P, Loutfi A, Liden M. Computer aided detection of ureteral stones in thin slice computed tomography volumes using convolutional neural networks. Computers in Biology and Medicine. 2018; 97: 153-60.